ELSEVIER

Ceramics International 31 (2005) 621–629

CERAMICS INTERNATIONAL

www.elsevier.com/locate/ceramint

Microstructure and microtexture in laser-dressed alumina grinding wheel material

Abhijeet A. Khangar[a], Edward A. Kenik[b], Narendra B. Dahotre[a,c,*]

[a]*Department of Materials Science and Engineering, The University of Tennessee, 326 Dougherty Hall, 1512 Middle Drive, Knoxville, TN 37996, USA*

[b]*Microscopy, Microanalysis, Microstructures Group, Metals and Ceramic Division, Oak Ridge National Laboratory, Oak Ridge, TN, USA*

[c]*Materials Processing Group, Metals and Ceramic Division, Oak Ridge National Laboratory, Oak Ridge, TN, USA*

Received 22 July 2004; received in revised form 29 July 2004; accepted 20 August 2004
Available online 16 December 2004

Abstract

Alumina grinding wheels when laser dressed with a high-power laser induce change in the morphology of the wheel surface. The altered grain structure on the surface of the wheel gives laser dressing advantage over conventional mechanical methods. Morphological modification during laser dressing is strongly influenced by the microstructure formed during the rapid solidification process. Microstructure depends mainly on the cooling rates amongst many other factors related to the laser processing conditions. Using a two-color based pyrometer temperature measurement setup the cooling rates were estimated during the laser dressing process. Orientation imaging microscopy (OIM) was used to determine the grain orientations in the resolidified layer on the dressed surface. Cooling rates and the OIM combined, indicate a preferred orientation of grains along the (110) planes. This preferred orientation can be a reason for the formation of grains with multi-faceted surfaces having cutting edges and vertices, for grinding operation. OIM and cooling results also show existence of a competitive growth mechanism for the grains in the dressed layer.

Keywords: D. Alumina; Pyrometric temperature measurement; Orientation imaging microscopy; Solidification

1. Introduction

Surface processing of ceramics by laser offers potential advantages, such as precise control over high input of thermal energy at spatial levels, rapid processing speed and a unique modification of microstructure due to rapid heating, melting, solidification and cooling. Depth of laser energy penetration into the wheel surface is constrained by the laser travel speed and the power input. Increasing irradiation time will allow the laser energy to penetrate deeper into the material.

Previous experiments using a laser as a dressing tool for the Al_2O_3 grinding wheels resulted in modification of morphological features on the surface [1–3]. The undressed wheel is a sintered structure of abrasive alumina grains held in place by the low-melting point bond material. Depending upon the laser processing parameters used, melting (followed by resolidification) and/or vaporization resulted in change of surface topography (morphology and composition). Selective removal of material (bond material, abrasive grains or even the clogged metal chips) is possible. Refinement of grain size, densification of surface layer, and evolution of multifaceted grains with cutting edges and vertices were seen on the surface of the wheel due to interaction with laser energy as described in [1]. The morphological changes on the grinding wheel due to interaction with laser results in an increased grinding efficiency (grinding ratios) [2].

The X-ray diffraction (XRD) experiments indicated formation of crystallographic texture on the surface of dressed wheels. Identification of planar textures due to laser dressing is important as the (atomic) planar density is

* Corresponding author. Tel.: +1 865 974 3609; fax: +1 865 974 4115.
E-mail address: ndahotre@utk.edu (N.B. Dahotre).

0272-8842/$30.00
doi:10.1016/j.ceramint.2004.08.013

Nomenclature

C_p	specific heat at constant pressure (J/(kg K))
D	thermal diffusivity (m^2/s)
G	thermal gradient (°C/m)
ΔH_m	latent heat of fusion (J/kg)
I_a	absorbed laser beam intensity (W/m^2)
$\dot{q}$	extra heat term (ex: latent heat, etc.)
R	growth rate (m/s)
t_0	time at which data acquisition starts during temperature measurement in solidification (s)
t	time during solidification (s)
T	temperature (K)
T_m	melting temperature (K)
T_o	initial temperature (K)
v	laser beam travel velocity (m/s)
V_i	liquid/solid interface velocity (m/s)
y	distance in melt pool (m)
	Greek letters
κ_s	thermal conductivity of substrate (W/(m K))
ρ	density (kg/m^3)
τ_1	laser beam dwell time (s)

expected to influence the formation of the types of crystallographic planes, that in turn will have strong bearing on the grinding characteristics. Pole figure analysis used to study the possible crystallographic texture after laser dressing of the ceramic wheels [2,3], indicated preferential orientation along the (110) plane.

The mechanical properties of directionally solidified structures, such as the ones produced after laser dressing, are very sensitive to microstructure and crystallographic texture, which can vary with processing conditions. It is necessary to quantify fully the microscopic and crystallographic texture in order to predict the material performance. Pole figure analysis by X-ray diffraction is a standard and useful technique for measuring crystallographic texture, and provides information averaged over the diffraction volume. In order to evaluate the effect of surface texture produced in the laser-dressed alumina grinding wheel, on the overall grinding process, microtexture information is needed. Orientation Imaging Microscopy (OIM) [4] is used for this purpose in the present study. OIM gives phase specific crystallographic information. In OIM, the local orientations are obtained from Kikuchi patterns, in a manner similar for TEM, but are produced from the surface of a bulk sample. Hence the patterns can be obtained from much larger area on the sample surface, giving more global information regarding the microtexture present in the test sample.

The microstructure formed on the surface of the laser dressed wheel depends on the temperature gradient and cooling rate. These in turn depend on the heat input, which is a function of the laser power used for processing. Alumina being a ceramic material has a poor thermal conductivity as compared to metals; therefore it tends to retain the heat for a longer time. Furthermore, presence of original porosity in the alumina wheel reduces the thermal conductivity [5], resulting in heat dissipation at a much slower rate. Some of the properties of alumina are given in Table 1. Laser dressing results in a decrease in the amount of porosity in the resolidified layer on ceramic materials due to consolidation of the surface structure [6–8]. Thus, the estimation of cooling rate is important to have an understanding of the evolution of microstructure and texture on the surface during laser processing. There are many models for predicting the formation of various microstructures during several different rapid solidification processes [9–11].

The experimental determination of cooling rates is done in the present paper to study its effect on the solidification structure during laser dressing. An attempt is made to correlate the microstructure formed on the wheel surface after laser dressing to the cooling rates in order to understand the multi-faceted nature of grains found during previous analysis [1–3]. A two-colored pyrometer is used for the experimental calculations of the cooling rates during the process. Microtexture analysis is done by OIM, which can give the local orientation information from a large area of the surface.

2. Experimental

Commercially available 0.25 wt% chromia doped alumina grinding wheel pieces were laser-dressed with varying laser power. The chemical composition of the abrasive grain material in the grinding wheel is 99.52 Al_2O_3–0.05 Fe_2O_3–0.18 Na_2O–0.25 Cr_2O_3 (wt%). Chemical composition of the vitrified bonding system is as given in Table 2. A 2.5 kW Hobart continuous-wave Nd:YAG laser equipped with a fiber-optic beam delivery system was used for dressing Al_2O_3 grinding wheel. Laser powers varying from 400 to 1000 W were used for processing the wheel. Overlap between the laser passes was limited to less than 20%. Dressing of the entire surface was done by scanning the laser beam in parallel tracks at a linear speed of 250 cm/min on the surface. Elaborate experimental details of the laser dressing process are described in [1,3].

Table 1
Properties of ceramic alumina

Property	Value[a]
Thermal diffusivity, D (m^2/s)	1.24×10^{-6}
Latent heat of fusion, ΔH_m (J/mol)	1.049×10^6
Melting temperature, T_m (K)	2323
Density, ρ (kg/m^3)	3.848×10^3
Specific heat, C_p (J/(kg K)): $C_p(Al_2O_3) = 117.49 + (10.38 \times 10^{-3})T - (37.11 \times 10^{-5}/T^2)$ J/(mol K)	1389

[a] *Source*: http://www.ceramics.nist.gov/srd/summary/scdaos.htm [values are taken for higher temperature near the melting point (2050 °C) of alumina].

Table 2
Chemical composition (wt%) of vitrified bonding system

SiO_2	Al_2O_3	Fe_2O_3	TiO_2	CaO	MgO	Na_2O	K_2O	B_2O_3
71.53	13.48	0.45	0.20	0.61	0.43	4.36	3.79	5.15

2.1. Temperature measurement using pyrometer

A commercially available two-color optical pyrometer (Chino model IR-FBQ1H) was configured for the measurement of temperature during laser dressing of the alumina grinding wheels. The temperature range covered by this instrument is 600–1500 °C with a response time of 0.5 ms. The pyrometer was further calibrated to measure temperature up to 2000 °C. A commercial temperature transfer standard in the form of a rather slow response but highly accurate two-color pyrometer (Mikron Model M190V-TS, SN 033641, calibration certificate no. 7138) was used for calibration. This transfer standard is annually returned to its manufacturer for calibration against NIST traceable temperature standards, and has an absolute accuracy of 10 °C over the range 800–3000 °C. A special telescope was used to collect the light signal from the sample surface during processing. The optical filters on the Chino collection optics lacked adequate rejection of the very strong stray light from the laser at 1.064 μm (Nd:YAG laser wavelength). Therefore, a wavelength rejection filter with a rejection ratio of $1{:}10^6$ was added.

The telescope (collection optics) of the pyrometer was mounted on the motion system and is focused at the same spot as the laser beam. A flexible optical fiber was used between the collection optics, called telescope here, and the remaining pyrometer components, in order to locate pyrometer electronic components and as many optical components as possible, away from the heat and fumes from the processing region. The precisely controlled motions inherent in laser processing impose the requirement that data acquisition equipment configured to observe and record the processing, be synchronized with the motion system. A specially written visual basic program for this purpose, receives ''motion started'' and a ''laser shutter open'' signals from the motion system and records temperature whenever the laser shutter is open as long as motion continues. Temperature versus time plots, are directly plotted during the laser dressing process, from which the cooling rates are estimated.

When processing ceramics at higher laser powers, a big plume is observed on the sample surface, which interferes with the signal intensity of light collected. This plume emits a white light and hence use of a single filter in the collection optics, to reject it is not possible. The plume causes saturation in the collected signal giving erroneous results. Thus, to overcome the problem due to plume, and to measure instantaneous temperature data directly at the spot where laser had been positioned, a delay of 5 s was given for the fly back of the laser before processing the next track. During this time the laser stays at the end of the processed track and the laser shutter remains off, but the data collection from the pyrometer continues, so as to record temperature data continuously at that spot as the sample cools. As the plume effect gradually disappears after the laser beam is turned off, the pyrometer starts recording real time temperature data. However, for the high powers (1000 W in the present case), volume of the plume is very large and it exists for a longer time (>3 s) over the sample surface after the laser beam has been turned off, thus saturating the pyrometer detector. During this time the temperature of the sample dropped substantial (to ∼400 °C). For such a low temperature, the filtered pyrometer detector has very low sensitivity to record accurate temperature values. Although the OIM analysis is presented for the 1000 W sample, temperature data was recorded for the 400 and 500 W samples. At these power levels, the plume was small and short lived (<1 s), to not saturate the pyrometer detector for recording the accurate temperature data.

2.2. Orientation imaging microscopy

To generate good quality Kikuchi patterns from laser-dressed Al_2O_3 ceramics, samples were prepared in cross-section by wet polishing with standard SiC grinding papers (600, 800, 1200 mesh), followed by colloidal silica paste (2 μm grain size) and diamond paste (1 μm grain size) with water as a lubricant in the subsequent steps. Since the Al_2O_3 ceramic samples are non-conductive, the specimens were first carbon-coated to uniform thickness of 3 nm and grounded with a copper tape to the sample stage in the SEM.

Electron backscattered diffraction (EBSD) patterns which are also called backscattered Kikuchi patterns, were generated at 20 kV in a commercial Philips XL30 FEG SEM equipped with a TSL orientation imaging microscopy system [12–14] using a special CCD camera. OIM analysis was performed at the Oak Ridge National Laboratory, TN, USA. In order to obtain EBSD patterns, the sample was steeply tilted to about 70° from horizontal, i.e. 20° with respect to the incident electron beam in the SEM. The quality of the EBSD Kikuchi pattern is a function of this angle, the electron beam voltage, and the sample surface quality.

The electrons that produce the EBSD pattern are a small fraction of the total scattered electron signal. In order to subtract this background signal, a background image was obtained with the electron probe scanning and that image was subtracted from each acquired EBSD pattern prior to indexing. To produce crystallographic orientation map, the electron beam is scanned over a selected surface area and the resulting EBSD patterns are automatically indexed and the local orientation determined. A certain minimum dwell time (of the beam) is needed at each spot for sufficient signal/noise in the EBSD pattern to ensure correct indexing. This time, the size and spatial resolution (step size) of the OIM map determine the total acquisition time. Confidence index (CI) is used to judge the correct indexing and Image Quality (IQ) indicates the quality and sharpness of the individual EBSD patterns. These parameters, amongst others, depends on factors like

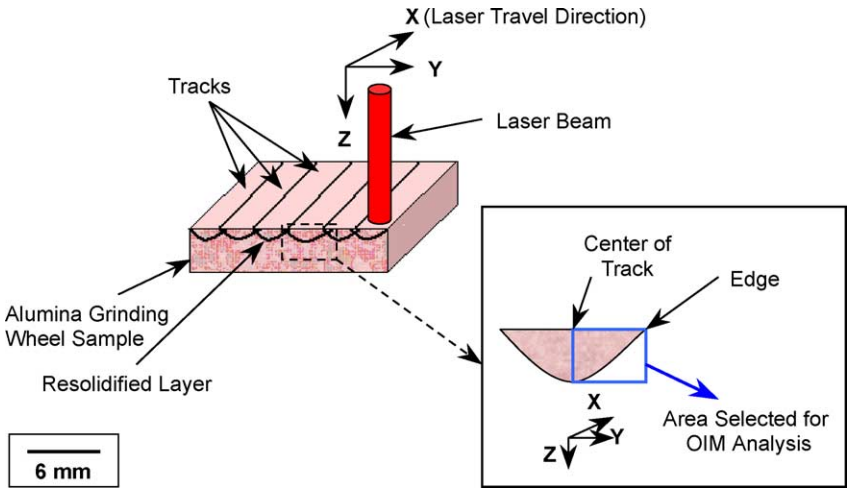

Fig. 1. Schematic of the alumina sample during laser dressing showing the laser beam travel direction (*X*-direction). The inset has one of the laser-dressed track (width ~3 mm) in cross-section showing the area selected for the OIM analysis.

crystal perfection in the diffraction volume, SEM and OIM system parameters [15,16], and hence is not an absolute value. For the present study a step size of 3.75 μm was used and the half of a track (from center to the edge of track as shown in Fig. 1) in the laser dressed sample (1000 W) was selected, covering the whole depth in the resolidified layer. From the X-ray and energy dispersive spectroscopic (EDS) analysis [1,2] it was found that the primary phase in the laser dressed sample was α-Al_2O_3 and hence the hexagonal crystal structure of alumina was selected to index the EBSD patterns obtained during analysis.

For the OIM analysis the 1000 W laser dressed sample is used, as at this higher power the depth of the resolidified layer was large enough for it be mounted and polished properly. Although, samples processed under different laser powers (400 and 500 W) are used for cooling rate calculations as in contrast to that used for OIM analysis (1000 W), the change in the processing power has a bearing only on the cooling rate, as discussed in the later section, and does not affect the trend in solidification behavior. As per the earlier observations [1–3], the microstructures obtained for all the processing powers used in present work, follow the similar trend in morphological features and an increase in laser power increased only the depth of the resolidified layer on the surface.

3. Results and discussion

Rapid solidification tends to show advantages such as refined microstructure and reduced microsegregation. In laser processing of materials, very high cooling rates are observed over a small region of workpiece where non-equilibrium microstructures are produced due to rapid solidification. A high heat input from the laser beam to melt in a localized area on the sample surface can achieve high cooling rates and the cooling rate will be different from center to edge of track causing a change in microstructure. Laser irradiation can be approximated as a point energy source on the surface, with heat flowing in all directions into the material being processed. The system can be assumed to attain a quasi-steady state when the travel velocity of the melt/solid interface becomes constant [17]. Incident radiation is partly reflected and partly absorbed by the material. Some amount of adsorbed energy is lost by re-radiation and convection, while rest is conducted into the substrate. The molten zone is heated from the surface at the center of the track (Fig. 1), which sets up convective currents inside the melt pool and provides fast dissipation of heat at the melt/solid interface.

The experimentally determined cooling rates during laser processing at two different powers (400 and 500 W) are given in Table 3. These are calculated from the temperature versus time data, as shown in Fig. 2, obtained directly from the experiments using the pyrometer. Curve fitting of the plots gives the time dependent equation for the temperature, the slope of which is the cooling rate. The fitted curve is extrapolated to the melting temperature of alumina to estimate the cooling rate near the melting point. It is assumed that the time versus temperature relation remains reasonably the same, as obtained in the range of temperature data acquisition. The actual data acquisition starts at time t_0 as indicated in the plots. This is due to the fact that the pyrometer requires some time to come out of saturation (after the laser beam is switched off) and start recording data. For the temperature versus time plots in Fig. 2, the scatter in the measured temperature data near the lower temperature range of the pyrometer is higher as compared to the upper range, due to an increase in the signal-to-noise ratio. This is due to a relatively low intensity of signal collected from the sample surface at lower temperatures compared to at higher temperatures. The cooling rate equations have a time term involved, and hence using these equations the cooling rate can be calculated at any time after the solidification starts. Data is given for two adjacent tracks

Table 3
Cooling rates results

Laser power (W)	Cooling rates (dT/dt) (°C/s)			
	Track 1		Track 2	
	Max dT/dt at melting temperature	dT/dt at a time, t = 2.2 s, after start of solidification	Max dT/dt at melting temperature	dT/dt at a time, t = 2.2 s, after start of solidification
400	−770.8	−437	−702.8	−382.8
500	−701.5	−401	−580.6	−299.7

and cooling rates calculated at the melting temperature (2050 °C) of alumina, which can be assumed to be the maximum cooling rate during the process, and also at a time 2.2 s after solidification starts, corresponding the lower calibrated temperature range (∼850 °C) of the pyrometer. The cooling rates obtained in sample processed at higher laser power are lower as compared to that of the ones at lower power. This can be explained from the fact that; being a poor conductor of heat, alumina tends to retain heat for a longer time as compared to metals. When other parameters such as alumina sample porosity, experimental environment, etc. remain same and the only factor changing is the laser beam power, an increase in heat input to the sample (i.e. increase of laser processing power) causes a greater heat build up, a larger melt zone and an increase in the interaction volume. Thus, it takes more time to dissipate this heat causing a drop in the cooling rates. Hence for further higher laser powers (like 1000 W), the cooling rate can be expected to be slightly lower as compared to that calculated for the lower power used (500 and 400 W).

Another notable observation is that the cooling rate in the second track is slightly lower than that in the first track for both the 400 W and the 500 W samples. As the laser passes over the first track, it preheats the adjacent material, resulting in a decrease in the thermal gradient, which in turn directly decreases the cooling rate for the second track. Table 3 also gives the cooling rate at the time of 2.2 s after solidification starts. This is the time when the corresponding temperature of the sample is near the lower calibrated temperature range of the pyrometer used for experimental temperature measurements. The trend observed in the cooling rate at this time is similar to that seen at the solidification temperature, but the cooling rates are much lower due to lower thermal gradients and heat loss from the sample. Solidification occurs in a direction opposite to that of heat extraction. As an assumption is made that the laser

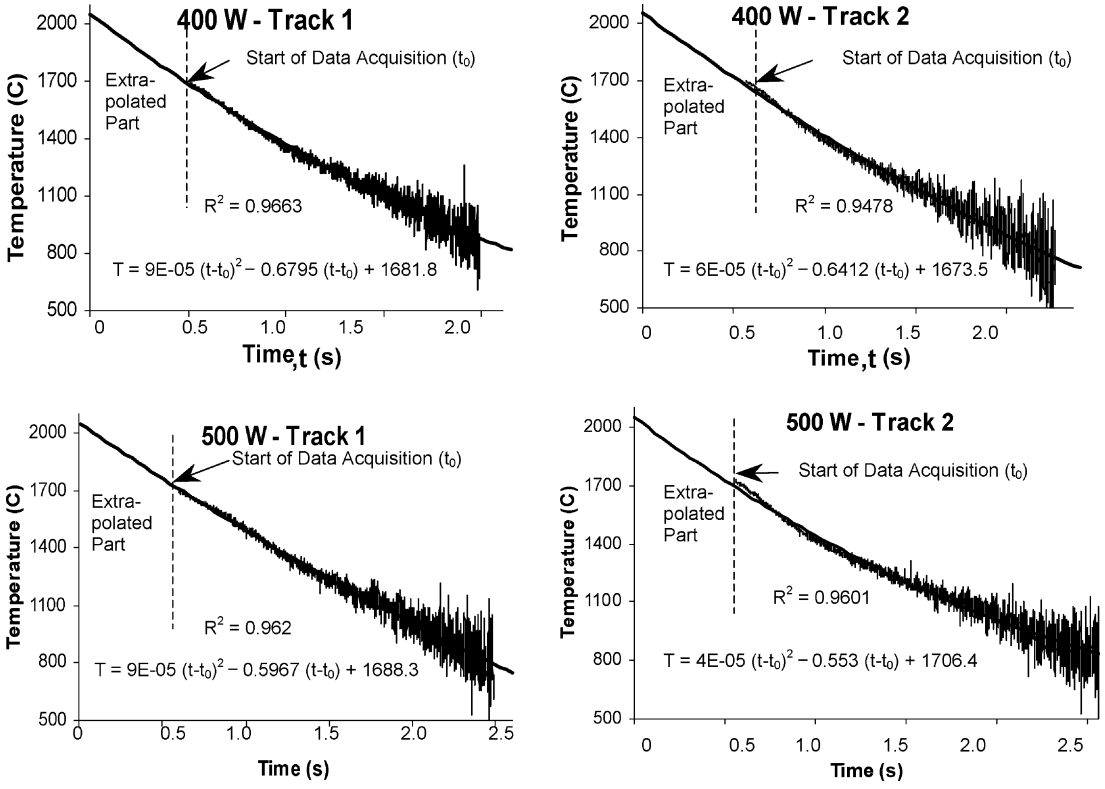

Fig. 2. Temperature vs. time plots obtained experimentally, for two tracks on the 400 and 500 W laser dressed samples.

Table 4
G/*R* ratios for various processing parameters

Part of track	*G*/*R* ratios for laser power:			
	400 W		500 W	
	Track 1	Track 2	Track 1	Track 2
Center	4.43×10^6	4.04×10^6	4.03×10^6	3.34×10^6
Edge[a]	1.74×10^9	1.74×10^9	1.74×10^9	1.74×10^9

[a] As Eq. (4), which is independent of *G*, is used for calculating the growth rate (*R*) near the edge, i.e. at the start of solidification, the *G*/*R* ratios for the edge are of the same magnitude for all the processing powers.

acts as a point source for energy input on the surface of sample and heat is extracted in all directions into the material being processed, it is expected that grain growth and the microstructure formed during solidification will be in accordance to this heat extraction model.

A range of microstructures (such as planar, cellular and dendritic) which are observed in laser processed materials are due to the different solidification conditions present [18,19]. A planar solidification front is observed when the interface is exactly at the equilibrium liquidus temperature and when every point in front of the interface is above the liquidus temperature. Thus, any instability formed on the interface dissolves back into the liquid. If melt is supercooled in front of the interface then any instability or perturbation formed on the interface will grow fast into the supercooled liquid. Under a positive temperature gradient, constitutional supercooling is solute driven. The ratio of *G*/*R*, where *G* is the thermal gradient and *R* is the solidification rate, governs the type of solidification structure formed during constitutional supercooling [18,19].

When the Al_2O_3 ceramic grinding wheels are subjected to laser energy, the sample surface melts and resolidifies causing a change in the surface morphology. The solidification structure in a single track varies with distance from the center of the track (which is along the *Y*-direction in Fig. 1). As shown in Fig. 3, at the center of the track, grains are multifaceted and equiaxed having a dendritic structure on them; whereas at the edges or the region of overlap between two adjacent tracks, the grains are elongated in shape (columnar) with growth taking place in a direction (*Y*-direction) normal to the laser beam travel. The columnar structures observed after laser dressing are similar to those previously reported by other workers [20–22] who have treated Al_2O_3-based ceramics with laser. During laser processing heat is continuously supplied to the surface at center of the track and hence the first regions to solidify are near the melt/solid interface away from the heat source, and as the laser beam moves further, the center as well follows suit.

The general heat transfer equation for a moving heat source, is given by the following equation in which the 'substantial derivative' of temperature [a function of position and time, i.e. $T = T(y, t)$] is given by the partial derivatives [23–26].

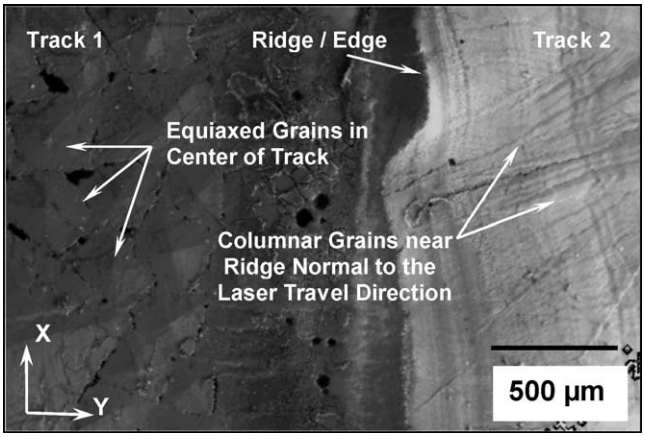

Fig. 3. SEM image showing columnar growth near the edges and equiaxed grains with dendritic structure in the center of the track.

$$\frac{\mathrm{d}}{\mathrm{d}t}[T(y,t)] = \frac{\partial T}{\partial t} + \frac{\partial y}{\partial t}\frac{\partial T}{\partial y} = D\frac{\partial^2 T}{\partial y^2} + \frac{\dot{q}}{C_\mathrm{p}\rho} \quad (1)$$

For time independent situation, i.e. quasi-steady state heat transfer for moving origin problem, the time-derivative of temperature tends to zero in Eq. (1). Hence, the surface-cooling rate $\mathrm{d}T/\mathrm{d}t$ in the direction opposite to laser traverse under quasi-steady state ($\partial T/\partial t = 0$) can be estimated as per quasi-steady state relation [25]:

$$\frac{\mathrm{d}T}{\mathrm{d}t} = \frac{\mathrm{d}T}{\mathrm{d}y}\frac{\mathrm{d}y}{\mathrm{d}t} \quad \text{or} \quad G = \frac{1}{v}\frac{\mathrm{d}T}{\mathrm{d}t} \quad (2)$$

where *v* is the laser beam travel velocity. Thus, the thermal gradients (*G*) are calculated from the temperature versus time plots assuming quasi-steady state using Eq. (2).

During solidification, the velocity of the liquid/solid interface or the growth rate (*R*) is given by the Neumann solutions to the Stefan Problem [27]. Assumptions are made that there exists strong convective currents in the melt pool and that the total energy absorbed at the free surface of the

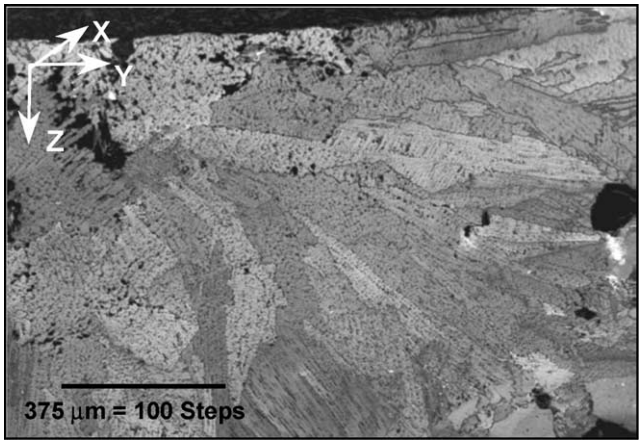

Fig. 4. Image Quality (IQ) cross-sectional image of the resolidified region within a track of the 1000 W laser dressed sample using OIM.

liquid is instantaneously transported to the interface by convection. The solution to Stefan problem is:

$$V_i \rho \Delta H_m - \kappa_s \frac{\partial T}{\partial y} = V_i \rho [\Delta H_m + C_p (T_m - T_o)] = I_a \quad (3)$$

where V_i is the liquid/solid interface velocity, and y distance in melt pool. This equation gives the average velocity of the interface during the time that the treated zone solidifies. The solidification front velocity (in the initial phase, i.e. at the start of solidification) is greater than the Eq. (3) estimates. At the start of solidification, the local temperature gradient is very large and this leads to maximum interface solidification velocity, which is approximated by [27]

$$V_i^{max} \approx \varsigma \left(\frac{D}{\tau_1} \right)^{1/2} \quad (4)$$

where τ_1 is the laser beam dwell time and ς is given by the solution of

$$\varsigma [1 + \mathrm{erf}(\varsigma)] \exp(\varsigma^2) = \frac{C_p (T_m - T_o)}{\pi^{1/2} \Delta H_m} \quad (5)$$

It is seen from the above equations that the average and the maximum interface solidification rates are highly dependent on the laser beam intensity and traverse speed.

Using Eqs. (3) and (4), respectively, the travel velocity (V_i) of solid/liquid interface, i.e. the growth rate (R) is calculated for the center of the track, and the edge where a maximum growth rate is observed, as the solidification front approaches the center of the track from the edge. Using the G and R values thus obtained, the G/R ratios are calculated and given in Table 4. The ratios are very high near the edge of the

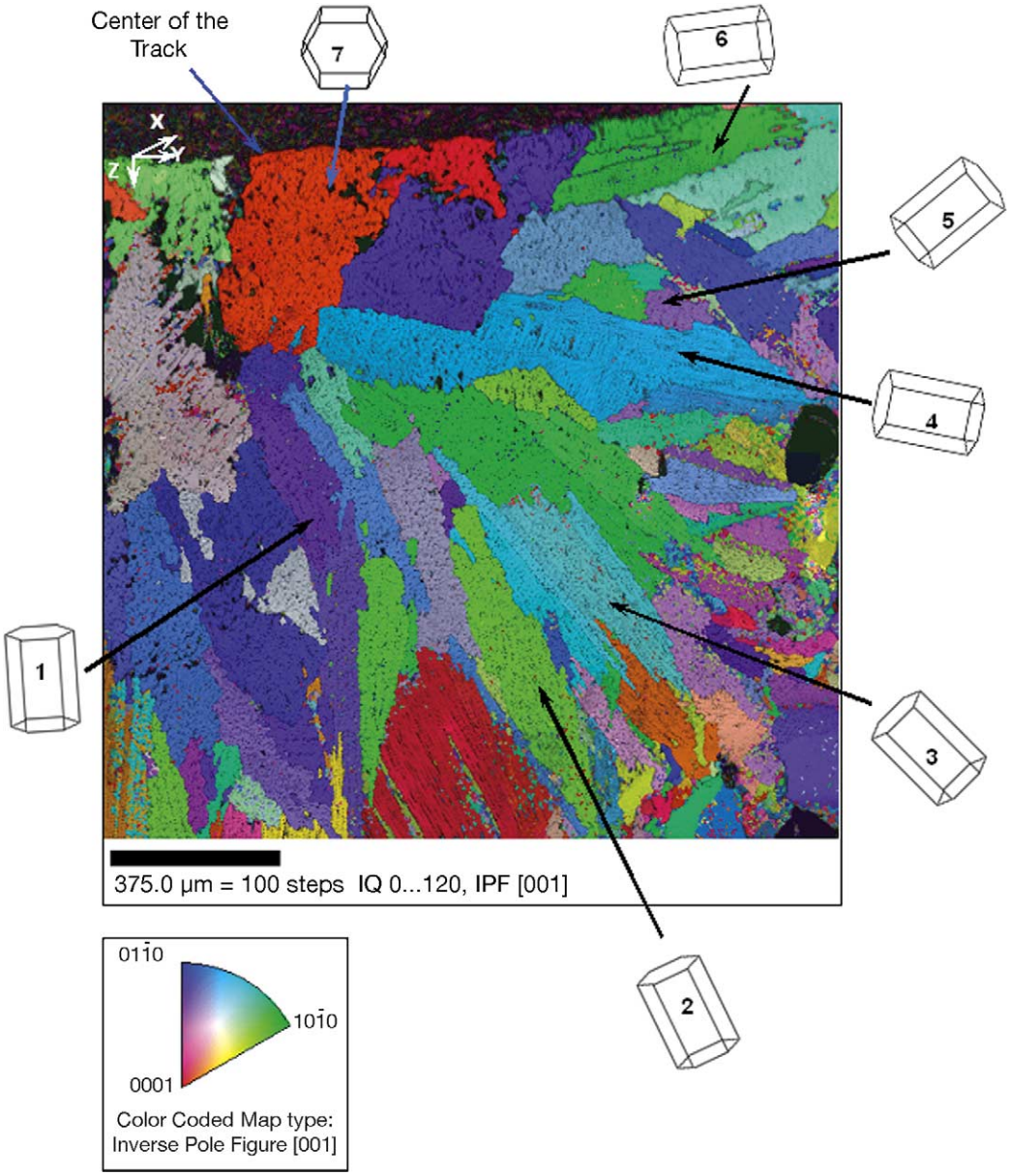

Fig. 5. Inverse Pole Figure (IPF) color-coded map of the selected resolidified area (in cross-section) on the laser-dressed (1000 W) grinding wheel.

track where the solidification starts and decrease towards the center. As Eq. (4) is used for calculating the growth rate (R) near the edge, i.e. at the start of solidification, the G/R ratios for the edge are of the same magnitude for all the processing powers. It is interesting to note that the solidification structure observed within a laser track varies from equiaxed grains with dendritic structure at the center of the track, to columnar grains near the edge (Fig. 3). Constitutional supercooling theory predicts that, increasing the G/R ratio causes a progressive change in the solidification characteristics, from fully dendritic to cellular-dendritic, to cellular and finally to planar. As mentioned above, similar trend in G/R is observed within a laser track. Thus, the actual microstructure observed is in accordance with the theory.

Fig. 4 is the image quality (IQ) image obtained from OIM. The area selected here is a cross-section of the resolidified layer in one of the tracks. Only half of the track was selected from center (inset in Fig. 1) to the edge towards right with proper care that the entire depth of the resolidified layer is mapped for OIM. Such an area was selected as a compromise between the total scan time required for OIM and the pixel spacing that determined the spatial resolution of the OIM maps at this magnification. IQ represents the sharpness of the EBSD pattern and thus local crystal perfection, therefore the IQ map reproduces the real microstructure as in conventional scanning or optical microscopy. The completely dark regions in this map are pores, where the value of IQ is essentially zero. Similarly, grain boundaries and other defects are easily detectable as seen in Fig. 4. This is in sharp contrast to the secondary electron image, which does not resolve any grain boundaries at that particular magnification. The growth direction of grains is radial from the free surface at the center of the track where the beam was focused (Fig. 4).

Fig. 5 is the Inverse Pole Figure (IPF) map of the same area as in Fig. 4. In an IPF map, the grains are color-coded for the crystallographic orientation of the local surface normal. The key for the color-coding is given in the stereographic triangle at the bottom. The orientations of some of the grains in the figure are shown in the form of the hexagonal cell for α-alumina. It is very clear from the figure that during solidification, growth takes place along the c-axis in the hexagonal α-alumina when subjected to laser irradiation. The grains 1–4, have an orientation radially outward from the center of the track as predicted by the heat extraction model. These are the grains, which lie within the resolidified layer. For the grains that are on the surface but away from the center of the track (grain 6 in Fig. 5), the orientation of cell is parallel to the surface but normal (in Y-direction) to the direction of laser travel (X-direction) in a track. For grain 7, which lies exactly at the center of the track, the cell orientation is along the surface but in a direction opposite to the laser travel direction.

There are some smaller grains in the resolidified layer (like grain 5) which have their c-axis differently oriented and not along the direction radially outward from the center of the track. It is seen that such grains do not grow in size as compared to the others (grains 1–4, 6, 7). Thus, a competitive growth mechanism is observed in which growth is very fast for the grains that have their c-axis parallel to the growth direction, where as the growth rate for all other grains is relatively slow. XRD and Pole figure analysis during earlier studies [2,3] indicated a preferred orientation for the (110) plane (Fig. 6). These are the prismatic planes, which are parallel to the c-axis in the hexagonal alumina cell. OIM maps suggest that, growth is taking place along the c-axis direction, which would favor (110) planes.

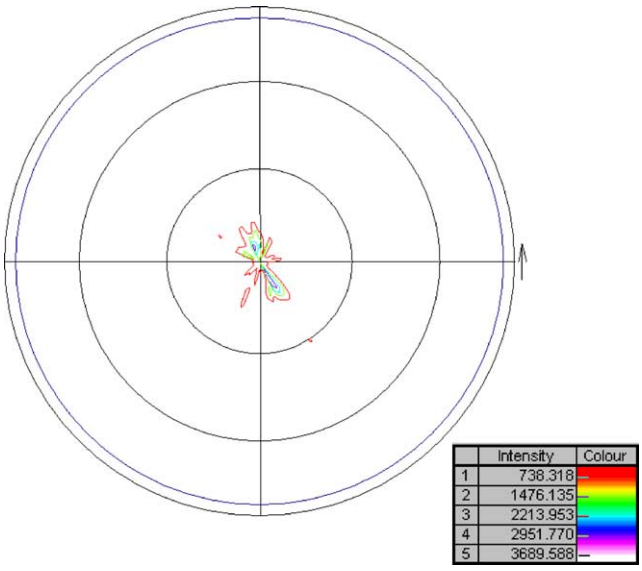

Fig. 6. X-ray pole figure for (110) plane in 1000 W laser-dressed sample.

4. Conclusion

Cooling rates of the order of $\sim 10^2$ °C/s are observed during the laser dressing of alumina grinding wheels. For the higher laser power processed samples the cooling rates are lower as compared to that of the samples processed at lower powers. Also, as the sample gets preheated, the cooling rate for second adjacent track is lower, due to lower thermal gradient. In the direction normal to the laser travel, solidification structure changes from equiaxed grains with dendritic structure at the center of track, to columnar near the edges. Using a proper polishing protocol, it was possible to get good quality EBSD patterns from the ceramic Al_2O_3 samples, permitting OIM analysis. The results show a preferred growth of grains along the c-axis and in a direction opposite to the heat flow. Further, OIM results in complement with XRD and pole figure analysis, suggests a preferred orientation of grains on the (110) planes, which are parallel to the c-axis in the hexagonal alumina cell. A competitive growth of grains takes place in the resolidified layer, during which the grains with c-axis not oriented

radially from the center of the track are suppressed in their growth.

Acknowledgements

The authors thank Dr. Mark J. Jackson of the Tennessee Technological University for introducing to this area of research. Dr. Joseph E. Spruiell's (University of Tennessee–Knoxville [UTK]), guidance for performing Pole figure analysis was very helpful. We highly appreciate the access to the orientation imaging microscopy facility at the Oak Ridge National Laboratory through the SHaRE User Center sponsored by the Division of Materials Sciences and Engineering, U.S. Department of Energy, under contract DE-AC05-00OR22725 with UT-Battelle, LLC. We also thank James O. Hornkohl, Fred Schwartz and Newton W. Wright (Center for Laser Applications, University of Tennessee Space Institute) for their help and support for the temperature measurement experiments. Dr S. Nayak and Anshul Singh (UTK) were great support during the research.

References

[1] M.J. Jackson, G.M. Robinson, N.B. Dahotre, A. Khangar, R. Moss, Laser dressing of vitrified aluminum oxide grinding wheels, Br. Ceram. Trans. 102 (6) (2003) 237–245.
[2] A. Khangar, N.B. Dahotre, Morphological modification in laser-dressed alumina grinding wheel material for microscale grinding, J. Eng. Mater. Technol., submitted for publication.
[3] A. Khangar, N.B. Dahotre, M.J. Jackson, G. Robinson, Laser dressing of alumina grinding wheels, in: N.B. Dahotre, R.J. Gaster, R.A. Hill, O.O. Popoola (Eds.), Heat Treating and Surface Engineering Congress & Exposition 2003, ASM International, Materials Park, OH, 2003, pp. 423–426.
[4] D.J. Dingley, V. Randle, J Mater. Sci. 27 (1992) 4585.
[5] D. Triantafyllidis, L. Li, F.H. Stott, Surface treatment of alumina-based ceramic using combined laser sources, Appl. Surf. Sci. 186 (2002) 140–144.
[6] J. Lawrence, L. Li, J.T. Spencer, The effects of high-power diode laser radiation on the wettability, adhesion and bonding characteristics of an alumina/silica-based oxide and vitreous enamel, Surf. Coat. Technol. 115 (1999) 273–281.
[7] Y. Yuanzheng, Z. Youlan, L. Zhengyi, C. Yuzhi, Laser remelting of plasma sprayed Al_2O_3 ceramic coatings and subsequent wear resistance, Mater. Sci. Eng. A 291 (2000) 168–172.
[8] L. Bradley, L. Li, F.H. Stott, Flame-assisted laser surface treatment of refractory materials for crack-free densification, Mater. Sci. Eng. A 278 (2000) 204–212.
[9] W. Kurz, R. Trivedi, Trans. ASME 114 (1992) 450.
[10] A. Kar, J. Mazumdar, J. Appl. Phys. 61 (1987) 2645.
[11] M. Rappaz, S. David, J.M. Vitek, L.A. Boatner, Metall. Trans. A 20A (1989) 1125.
[12] D.J. Dingley, D.P. Field, Mater. Sci. Technol. 12 (1) (1996) 1–9.
[13] D.P. Field, Ultramicroscopy 67 (1) (1997) 1–9.
[14] B.K. Kim, J.A. Szpunar, Scripta Mater. 44 (2001) 2605.
[15] J.K. Farrer, J.R. Michael, C.B. Carter, in: A.J. Schwartz, M. Kumar, B.L. Adams (Eds.), Electron Backscatter Diffraction in Material Science, Kluwer Academic/Plenum Publishers, New York, 2000, p. 299.
[16] K.Z. Baba-Kishi, J. Mater. Sci. 37 (2002) 1715.
[17] J. Mazumdar, W.M. Steen, J. Appl. Phys. 51 (2) (1980) 941–947.
[18] M.C. Fleming, Solidification Processing, McGraw Hill, New York, 1974.
[19] O. Esquivel, J. Mazumdar, M. Bass, S.M. Copeley, Microstructural formation according to the theory of constitutional supercooling, in: R. Mehrabian, B.H. Kear, M. Cohen (Eds.), Rapid Solidification Processing, Principles and Technologies II, Claitors, Baton Rouge, 1980, pp. 150–173.
[20] L. Bradley, L. Li, F.H. Stott, Appl. Surf. Sci. 138–139 (1998) 522–528.
[21] S.Z. Lee, K.H. Ghar, Mat. Wiss. Wekstofftech. 23 (1992) 117–123.
[22] J.H. Shieh, S.T. Wu, Appl. Phys. Lett. 59 (1991) 1512–1514.
[23] D. Rosenthal, Welding J. Suppl. 20 (1941) 220–234.
[24] D. Rosenthal, Trans. Am. Soc. Mech. Eng. 68 (1946) 849.
[25] H.S. Carslaw, J.C. Jaeger, Conduction of Heat in Solid, Clarendon Press, Oxford, 1962.
[26] S. Kou, R. Mehrabian (Eds.), Modeling of Casting and Welding Processes III, The Metals, Minerals and Materials Society, TMS, Warrendale, PA, 1986.
[27] D. Bäuerle, Laser Processing and Chemistry, third ed. Springer, Berlin, 2000, pp. 168–176.